Analysis of Reader Orientation on Detection Performance of Hilbert Curve-based Fractal Chipless RFID Tags

Muntasir M. Sheikh

King Abdulaziz University, Department of Electrical and Computer Engineering
Jeddah 21589, Saudi Arabia
mshaikh@kau.edu.sa

Abstract – The role of the orientation of the radio frequency identification (RFID) reader is vital in the RFID-based communication system. This study presents the design and analysis of the impact of the orientation of the RFID reader (angle of incidence of the plane wave) on the detection and sensitivity characteristics of fractal chipless RFID tags. Four fractal (irregular) shaped tags are developed using four iterations of the Hilbert curve filling algorithm. The full-wave EM analysis of the designed tags in Matlab is performed by exporting them in Computer Simulation Technologies Micro-Wave Studio (CST MWS) in the frequency range of 2 to 20 GHz. Firstly, the performance of the tags is analyzed by observing the radar cross-section (RCS) of the tag for the fixed orientation of the incident plane wave in three different polarizations (horizontal, vertical, and oblique). Later, the variations in the EM spectrum (RCS results) are analyzed for oblique polarization by varying the incidence plane wave in both elevations (for two cases of 0° and 90°) and azimuth planes (sweeping from 0° to 180° with a step size of 10°). The analysis of the proposed aggregated RCS response for all cases in oblique polarization produces higher coding capacity (169 bits), coding spatial capacity (16.504 bits/cm^2), coding spectral capacity (9.826 bits/GHz), and coding density (0.960 bits/GHz/cm^2) for the realized highly irregular tag using fourth-iteration (4T) of Hilbert curve filling algorithm. The proposed procedure of detection based on aggregated response makes the developed RFID communication system more secure and reliable.

Index Terms – Angle of incidence, chipless RFID, coding den, fractal tags, RFID readers.

I. INTRODUCTION

The popularity of chipless radio frequency identification (RFID) tags has increased over the last decade. Chipless RFID tags are the vital components of a wide range of modern-day applications such as warehouse inventory management, logistics, bio-medical, Internet of Things (IoT), and document security [1–3].

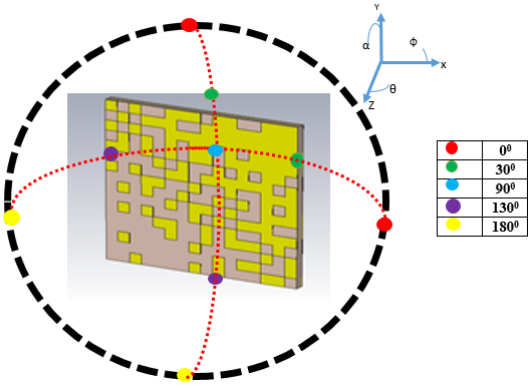

Fig. 1. Analysis framework for different orientations (angle of incidences of illuminating plane waveform of RFID reader on Hilbert curve-based fractal tag).

The action of a chipless RFID tag is based on the backscatter from the tag due to the incident signal from the RFID reader. The RFID reader decodes the features of the backscattered signal which leads to its unique identification. The backscattered signal contains the resonance frequency features (dips or notches) of the tag which are analyzed using both time and frequency domain techniques [4, 5]. Frequency domain tags use the amplitude and phase of the reflected signal or radar cross-section (RCS) of the tag for its characterization and identification [3, 5–7].

Different resonance structures [3, 5, 8–10] of the RFID tags are reported in the literature for different applications. The conventional tag structures [3, 5, 8–10], although providing good performance in terms of coding density, lack in the development of a secure and safe wireless communication system [11, 12]. The scattered tag information could be intercepted and decoded by predators.

Fractal chipless tags have emerged as a good solution to this problem as their resonance characteristics cannot be easily interpreted by a conventional RFID reader due to their inherent irregular structures [7, 13–15]. The commonly reported techniques for the

Submitted On: October 6, 2022
Accepted On: April 2, 2023

https://doi.org/10.13052/2024.ACES.J.390603

generation of fractal tags are fragmented loaded resonators [14], space-curve filling [12, 16–18], the game of life theory [11], irregular natural geometries [7], and shape-optimized fractal structures [19].

Space-filling curved (Peano and Hilbert curves) based RFID tags have compact structures and offer higher encoding densities which depend on the layout of the curves [17]. The developed geometries have an iterative nature and their planar structures offer the additional advantage of cheaper fabrication. Murad et al. [16] developed Hilbert-curve antennas for RFID applications at 2.4 GHz. The authors in [17] proposed RFID tags based on the array of Peano and Hilbert curve elements. Dual band Card-type Hilbert-curve fractal antenna for high and ultra-high frequency range RFID applications is reported in [15].

This study reports a detailed simulation of the impact of the RFID reader orientation on the backscattering of designed Hilbert curve-based fractal RFID tags. Four different irregular-shaped RFID tags are developed using the Hilbert curve filling algorithm in Matlab. The designed tags are then imported into CST MWS using the Matlab-CST API. The 3D geometries of the tags with added FR4 substrate in CST are analyzed in the frequency range of 2 to 20 GHz.

Each tag geometry is illuminated by a plane wave, and its backscattered RCS responses are recorded for the fixed and varying orientations of the illuminating plane wave. For the fixed orientation, all tag RCS results are analyzed in three different polarizations (horizontal, vertical, and oblique). In the second case study analysis, the incident plane wave angle of incidences is varied in both the elevation and azimuth planes, and RCS results are recorded for oblique polarization. Here two different configurations of elevation plane angles, i.e. φ=0° and $\varphi = 90°$ are chosen for the analysis purpose. For each configuration of elevation angle, the azimuth angle (θ) is changed from 0° to 180°, and RCS waveforms are recorded for each case. Figure 1 illustrates the concept of the different angles of incidence of a plane wave (mimicking the different orientations of the RFID reader) on one of the designed fractal tags. Next, aggregated RCS responses for both cases of elevation plane, i.e. $\varphi = 0°$ (case 1) and $\varphi = 90°$ (case 2) are considered to analyze the overall coding performance of tags in terms of coding capacity (bits), coding spatial capacity (bits/cm^2), coding spectral capacity (bits/GHz), and coding density (bits/GHz/cm^2). The details of the design procedure, the EM analysis of realized tags, and the analysis of the tags for the configurations are given in the next sections.

Since there was no fabrication of the tags or experimental validation of the simulation results, we used the same numerical setup that was used in similar previous papers [3, 7] where simulations were validated by experimental results. This gave us confidence that our simulation produces credible results. We intend to fabricate the tags designed in this paper and experimentally validate our results soon.

II. DESIGN OF FRACTAL TAGS

The Hilbert curve filling technique is used for designing different irregular-shaped tags for the proposed study. Four tags are designed using different iterations of the Hilbert curve filling algorithm in MATLAB and then are imported to CST MWS for full-wave EM analysis. The details for the design and implementation steps in MATLAB are as follows:

- CST-MATLAB application interface (API) is installed on the system.
- Develop the Hilbert curve filling algorithm in MATLAB.
- Design the different 2-dimensional (2D) tag shapes in MATLAB by using the developed Hilbert curve filling algorithm.
- Import the designed 2D image into CST MWS using the integrated CST-MATLAB API.

After the first iteration (1T) of the Hilbert space-curve filling, a 2D image is created in MATLAB. Figure 2 (a) depicts the tag's shape after the 1T of the Hilbert curve filling algorithm. The 1T of the algorithm produces only a rectangular-shaped tag.

The second (2T), third (3T), and fourth (4T) iterations of the tag can also be generated, as shown in Figs. 2 (b-d). We note from Figs. 2 (b-d) that the tag shape becomes more irregular in each successive iteration.

A. Simulation environment

The tags designed in MATLAB are imported into CST MWS as a 3D shape using the CST-MATLAB API for the full-wave EM analysis. The full pack of an API is required for the successful interfacing of MATLAB and CST.

Figure 2 depicts the 3D executed tags in CST with the addition of the substrate behind the 2D tag geometry. Each 2D shape of the tag is placed on an FR4 substrate of 32x32x1.6 mm. The 2D tag shape is assigned to copper material with a thickness of 0.04 mm. The horizontal, vertical, and oblique polarization electrical field probes are placed in the far-field region at 140 mm. The far-field distance (z) satisfies the condition of $z>2D2/\lambda$, where D depicts the size of the tag and λ refers to the free-space wavelength at 20 GHz. These probes are used to record the RCS of each tag for all analyzed cases of angular reader orientations. The RCS analysis of all tags is performed in the frequency range of 2-20 GHz.

Each tag geometry is illuminated with the incident plane wave at different angles of incidence, mimicking the angular nature of the reader. Figure 3 presents the

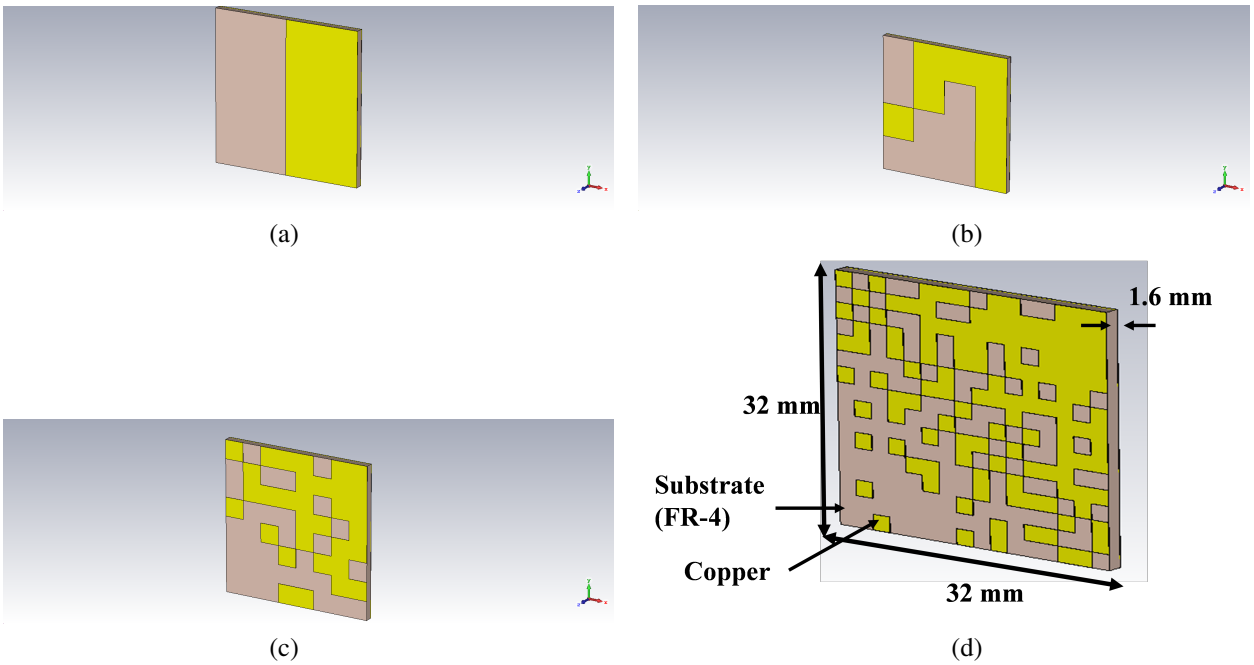

Fig. 2. Designed CST and Matlab structure of applied Hilbert curve filling on the chipless RFID tags: (a) Tag 1 (1T), (b) Tag 2 (2T), (c) Tag 3 (3T), and (d) Tag 4 (4T).

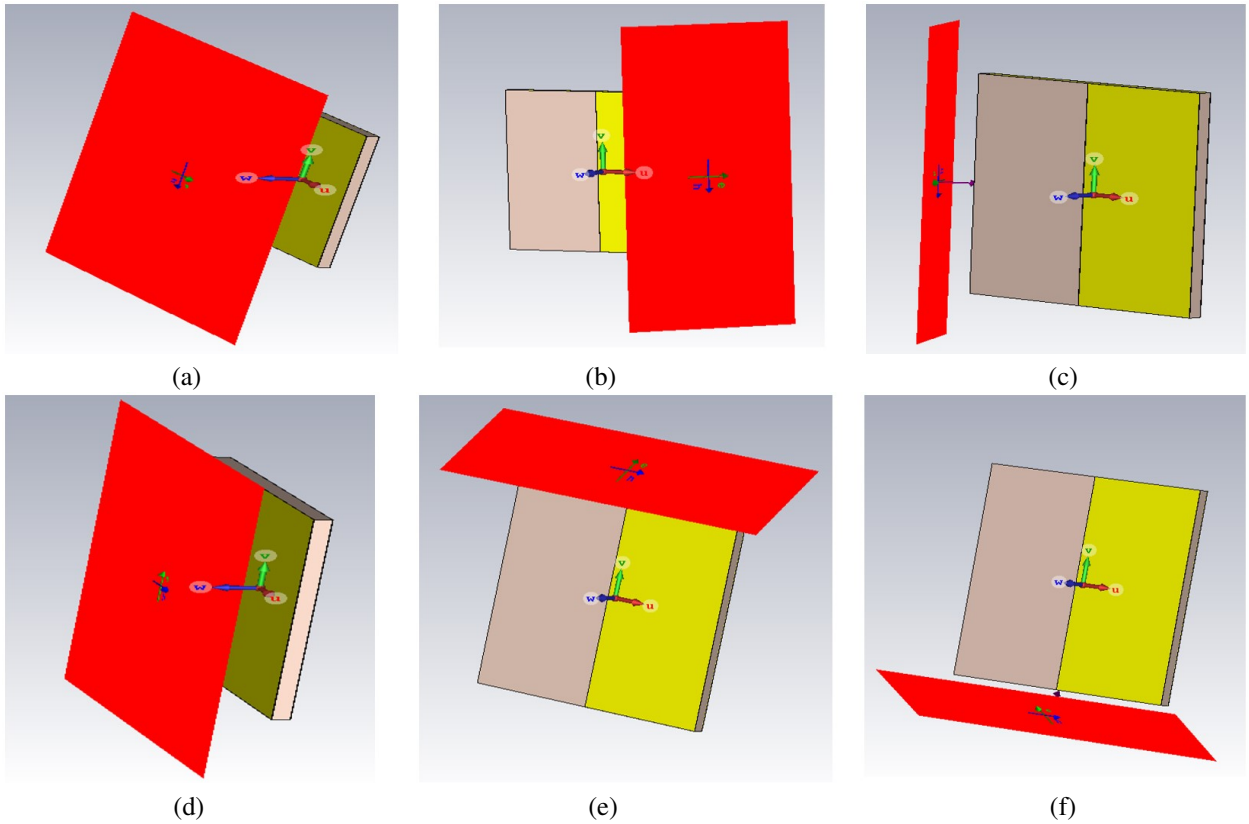

Fig. 3. Tag 1 (1T) with different angle of incidence of plane wave excitations: (a) $\varphi = 0°, \alpha = 0°$, and $\theta = 0°$; (b) $\varphi = 0°$ $\alpha = 0°$, and $\theta = 50°$; (c) $\varphi = 0°, \alpha = 0°$, and $\theta = 150°$; (d) $\varphi = 90°, \alpha = 0°$, and $\theta = 0°$; (e) $\varphi = 90°, \alpha = 0°$, and $\theta = 50°$; (f) $\varphi = 90°$, $\alpha = 0°$, and $\theta = 140°$[11].

selective cases of the different angles of incidence of the angular reader for Tag 1 [11]. Figure 3 (a) refers to the plane wave excitation with φ=0°, α=0°, and θ=0° which represents the case of zero elevation and azimuth angles of the RID reader. The cases of change in azimuth angles to 50° and 150° of the RFID readers are shown in Figs. 3 (b-c) with the fixed elevation orientation of 0°. Figures 3 (d-f) show the simulation environment with a fixed elevation angle of 90° for plane wave excitation (reader orientation) with the change in azimuth angles to 0°, 50°, and 140°, respectively.

The incident plane wave elevation angle (φ) of the angular reader is chosen to be 0^o and 90^o for this study. For each elevation angle, the value of the azimuth angle (θ) of the incident plane wave is changed from 0^o to 180^o with a 10^o step size, as illustrated in Fig. 1 and some selective cases in Fig. 3. The incident elevation angle (φ) configurations of 0^o and 90^o are referred to as case 1 and case 2 for brevity in the onward discussion. Table 1 summarizes the analyzed reader orientation cases.

Table 1: Analysis cases of angular reader orientations

	Reader Orientation
Case # 1	$\varphi = 0°, \alpha = 0°$, and $\theta = 0 - 180° \, (10° \text{ step})$
Case # 2	$\varphi = 90°, \alpha = 0°$, and $\theta = 0 - 180° \, (10° \text{ step})$

The current distribution and RCS results are recorded and analyzed for each case of RFID reader incident angle for horizontal (HH), vertical (VV), and oblique polarization for the four different realized tags of Fig. 2 for each θ and φ combination.

III. ANALYSIS OF REALIZED TAGS WITH FIXED READER ORIENTATION

An RFID reader is a wireless transceiver that reads a code printed on a tag. The reader does not have to scan the tag directly or have a line of sight with it. However, the tag must be within the readers' range (typically 10-100 m) to be successfully read. The reader is a transceiver that utilizes an antenna to emit radiofrequency. There is no integrated circuit on a chipless tag. Instead, a unique pattern is printed or engraved on the tag. This pattern (code) is usually made by metallization on a dielectric (substrate). Thus, the metallization reflects the RF energy to the reader, which is programmed to identify the unique pattern. In this work, we study backscattered, frequency-domain, chipless RFID tags designed using Hilbert curve-based metallization. Specifically, we are studying the effect of RFID reader angular orientation on the encoding capacity of the tag. The analysis is performed for both fixed and angular rotations of the RFID reader.

First, the analysis of the different realized tags is performed in terms of their current distribution and RCS results for the three different polarizations (horizontal, vertical, and oblique) for the fixed reader orientation. The excitation plane wave is incident at fixed angles (H [horizontal]= $\varphi = 0°$, $\alpha = 0°$, and $\theta = 0°$, V [vertical]= $\varphi = 0°$, $\alpha = 90°$, and $\theta = 0°$, Ob [oblique]= $\varphi = 0°$, $\alpha = 0°$, and $\theta = 45°$) and the results for each tag are analyzed.

A. Surface current distribution analysis

Figures 4 (a-d) depict how the current distribution changes as the tag structure changes in horizontal polarization. These results correspond to Tag 1, Tag 2, Tag 3, and Tag 4 at resonance frequencies of 4.25 GHz, 8.16 GHz, 8.25 GHz, and 8.16 GHz, respectively. The RCS peaks can be easily identified by considering the noise level. The used level of noise is around 5-10 dB, which is the difference between the lowest RCS value and the highest RCS value of resonant frequency. With the change in the fractal geometry, we observe significant variations in the spreading of the current around the metallic structures of the tag. The change of the irregular copper shape of the tag with each successive iteration of the Hilbert curve filling algorithm brings out the variations in the resonance characteristics of each tag, as evident from the results of Figs. 5 (a-d) for the fixed horizontal polarization for all tags.

The red color, which represents highly concentrated surface current areas, shows the most exciting parts of the tags at the selected frequencies. The metallic islands of the tags resonate at different frequencies depending on their size compared to the wavelength. The change in the tag's metallic structure varies its electrical size and thus changes its resonance characteristics. The observed maximum value of current J_{max} (corresponding to red color) is 0.114 A/m, 0.060 A/m, 0.106 A/m, and 0.275 A/m for Tag 1, Tag 2, Tag 3, and Tag 4, respectively, at their mentioned unique resonance frequencies.

The change in polarization significantly impacts the current distribution around the metallic islands of the fractal tags. This is observed when the tag's current distributions are analyzed for vertical and oblique polarization under the same settings as the incident plane wave. Figures 5 (e-h) illustrate the current distribution of the realized four tags for vertical polarization. The resonance frequencies of all tags changed to 6.9 GHz (1T), 7.85 GHz (2T), 19.42 GHz (3T), and 6.23 GHz (4T).

A similar observation in the tag's current distribution characteristics is observed for the oblique polarization. The results for the oblique polarization are depicted in Figs. 4 (i-l). The comparison of oblique polarization results with earlier cases confirms that the realized fractal tags are sensitive to polarization changes even with the

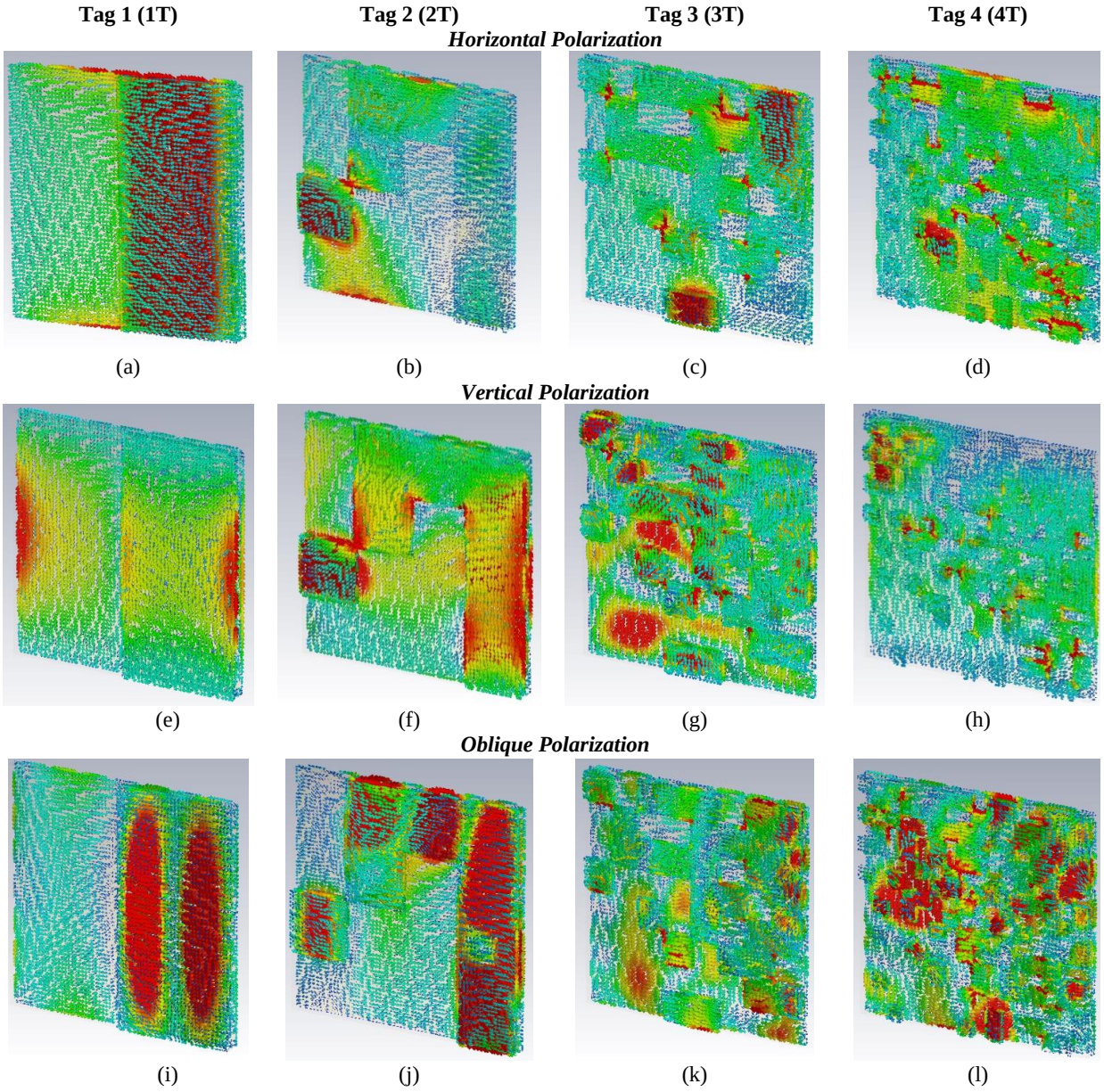

Fig. 4. Surface current distribution of realized chipless RFID tags (Tag 1, Tag 2, Tag 3, and Tag 4) of Fig. 2 with the plane wave illumination angle of $\alpha = 0^{\circ}$. (a) Horizontal polarization: 1T at $f = 4.25$ GHz, $J_{max} = 0.114$ A/m; (b) Horizontal polarization: 2T at $f = 8.16$ GHz, $J_{max} = 0.060$ A/m; (c) Horizontal polarization: 3T at $f = 8.25$ GHz, $J_{max} = 0.106$ A/m; (d) Horizontal polarization: 4T at $f = 8.16$ GHz, $J_{max} = 0.275$ A/m, (e) Vertical polarization: 1T at $f = 6.9$ GHz, $J_{max} = 0.038$ A/m; (f) Vertical polarization: 2T at $f = 7.85$ GHz, $J_{max} = 0.064$ A/m; (g) Vertical polarization: 3T at $f = 19.42$ GHz, $J_{max} = 0.042$ A/m; (h) Vertical polarization: 4T at $f = 6.23$ GHz, $J_{max} = 0.216$ A/m, (i) Oblique polarization: 1T at f=8.41 GHz, $J_{max} = 0.038$ A/m; (j) Oblique polarization: 2T at f=9.00 GHz, $J_{max} = 0.041$ A/m; (k) Oblique polarization: 3T at $f = 19.19$ GHz, $J_{max} = 0.030$ A/m; (l) Oblique polarization: 4T at f=18.78 GHz, $J_{max} = 0.041$ A/m.

fixed angle of incidence of the plane wave for all tags. Therefore, the significant changes in the resonance characteristics of the tag for each polarization increase the coding density of the tags.

B. RCS analysis

The RCS results of the four tags are analyzed for the three horizontal, vertical, and oblique polarizations for the fixed angle of the illuminating plane wave. Figure 5

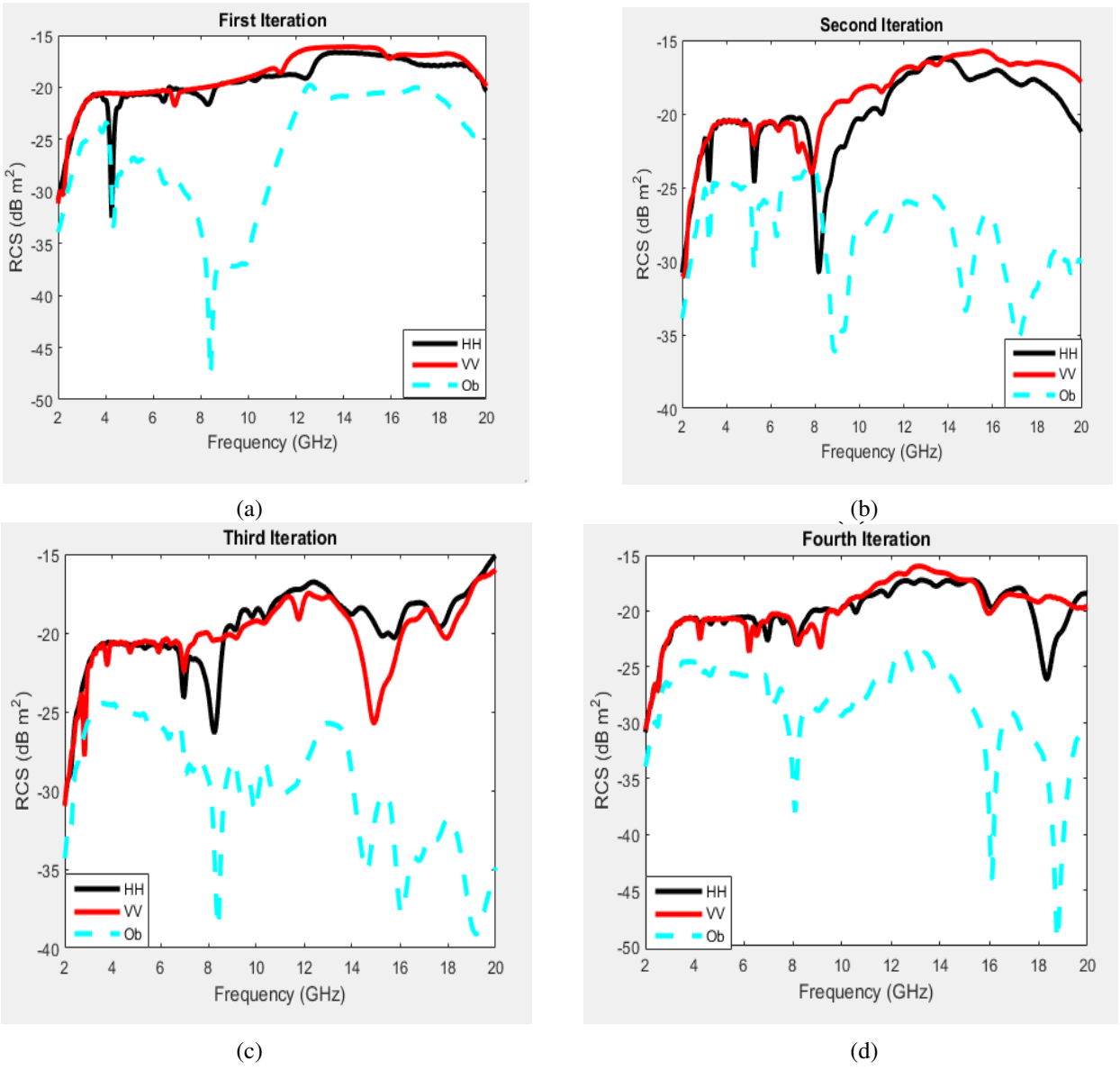

Fig. 5. RCS results of realized chipless RFID tags with the plane wave illumination angle of α=0^o: (a) 1T, (b) 2T, (c) 3T, and (d) 4T.

shows the obtained results of Tag 1, Tag 2, Tag 3, and Tag 4, respectively, in the three analyzed polarizations. The resonance frequencies of each tag can be observed from the dips in the respective waveform results horizontal (HH), vertical (VV), and oblique (Ob) polarizations. We observe that Tag 1 (1T) has resonance frequencies of 4.25 GHz, 6.43 GHz, 8.3 GHz, and 12.4 GHz in horizontal polarization; 6.90 GHz and 11.34 GHz in vertical polarization; and 4.34 GHz, 3.85 GHz, 6.48 GHz, and 8.41 GHz in oblique polarization, respectively. The difference in resonance characteristics in different polarizations is due to the change in the current distribution of the tags, as shown in Figs. 4 (a,e,i), respectively, for Tag 1. The performance of each tag is also analyzed in terms of the coding capacity (bits), coding spatial capacity (bits/cm^2), coding spectral capacity (bits/GHz), and coding density (bits/GHz x cm^2) of the tag.

For the fixed orientation case, the coding capacity is computed by adding all the resonant frequencies (dips in the analyzed RCS spectrum) for all polarizations (horizontal [HH] + vertical [VV] + oblique [Ob]) for the analyzed fixed orientation of the reader as shown in (1):

$$Coding\ Capacity_{fixed\ orientation} = \sum All\ resonance\ frequencies\ (HH+VV+Ob). \quad (1)$$

Table 2: Resonance frequency (in GHz) of characteristics of realized chipless RFID tags of Fig. 1 for fixed orientation of RFID reader

	Polarization		
Tag #	**HH**	**VV**	**Ob**
1	4.25, 6.43, 8.3, 12.4	6.90, 11.34	4.34, 3.85, 6.48, 8.41
2	3.21, 5.26, 6.32, 8.16, 11	5.26, 6.36, 7.24, 7.85	3.22, 5.26, 6.27, 9.00, 11.14, 14.80, 17.08
3	6.97, 8.25, 9.13, 9.83, 10.41, 15.27, 15.77, 17.71	2.83, 3.76, 4.74, 5.92, 6.99, 11.77, 19.42, 17.97	6.36, 7.10, 7.36, 8.41, 9.36, 9.94, 14.6, 16.08, 19.19
4	4.21, 4.64, 5.20, 6.55, 6.97, 7.96, 8.16, 10.57, 11.90, 16.09	4.23, 6.23, 6.54, 8.23, 9.13, 15.99	4.27, 7.11, 8.10, 9.06, 9.99, 10.84, 11.86, 12.91, 16.09, 18.78

Figure 5 (a) shows that for Tag 1, there are 4, 2, and 4 resonance frequencies in the HH, VV, and Ob polarizations, respectively, resulting in a coding capacity of 10 bits for the analyzed frequency range. The coding spatial capacity is computed by dividing the coding capacity by the tag area, as depicted in (2):

$$Coding\ Spatial\ Capacity = \frac{Coding\ Capacity}{Tag\ Area\ (cm^2)}\ . \quad (2)$$

The coding spatial capacity for Tag 1 comes out to be 0.997 bits/cm^2 (10/10.24). The division of coding capacity by the investigated frequency spectrum of dips (resonance frequencies) produces the coding spectral capacity (see (3)):

$$Coding\ Spectral\ Capacity = \frac{Coding\ Capacity}{GHz}\ , \quad (3)$$

$$Coding\ Density = \frac{Coding\ Capacity}{GHz \times Tag\ Area\ (cm^2)}\ . \quad (4)$$

The spectral range of resonance dips for Tag 1 is from 3.85 GHz to 12.4 GHz. Therefore, the coding spectral capacity becomes 1.170 bits/GHz (10/8.55). Lastly, with the help of (4), coding density can be calculated at 0.114 bits/GHz x cm^2 (10/8.55x10.24) for Tag 1.

The results of Tag 2 are depicted in Fig. 5 (b). The observed resonances for this case are 3.21 GHz, 5.26 GHz, 6.32 GHz, 8.16 GHz, and 11 GHz in horizontal polarization; 5.26 GHz, 6.36 GHz, 7.24 GHz, and 7.85 GHz in vertical polarization; and 3.22 GHz, 5.26 GHz, 6.27 GHz, 9.00 GHz, 11.14 GHz, 14.80 GHz, and 17.08 GHz in oblique polarization, respectively. We notice that the change in the tag metallic geometry with the second iteration brings a notable change in the resonance properties of the tag. Also, it is observed that 2T has more unique resonance frequencies as compared to 1T, which increases its coding capacity to 16 bits as to the 10 bits of the 1T tag. Similar observations regarding the enhanced coding capacities of Tags 3 and 4 can be made from the increased number of resonances in their RCS results in Figs. 4 (c) and (d), respectively. Table 1 summarizes the resonance frequency of all four tags in Fig. 5.

The comparison of different characteristics of the realized tags in terms of coding capacity (bits), coding spatial capacity (bits/cm^2), coding spectral capacity (bits/GHz), and coding density (bits/GHz x cm^2) is given in Table 1. We observe that Tag 3 exhibits a coding capacity of 25 bits in the resonance frequency range of 2.83-19.42 GHz. The resonance frequency range of the most complex shape Tag 4 is 4.21-18.78 GHz with the highest coding capacity of 26 bits. Tag 4 also has the highest values of coding spatial capacity (2.539 bits/cm^2), coding spectral capacity (1.784 bits/GHz), and coding density (0.174 bits/GHz x cm^2). These results infer that the increase in the number of iterations of the Hilbert curve filling algorithm makes the tag structure more irregular and thus increases its overall coding properties as compared to earlier iteration tags.

IV. ANALYSIS OF REALIZED TAGS WITH DIFFERENT READER ORIENTATION

The second case study is the investigation of the resonance and coding properties of the four realized tags in oblique polarization with the change in the horizontal angle (theta) of an incident plane wave in the range of 0-180° for two different cases in Table 1. At first (case 1), angles phi (φ) and alpha (α) are fixed at zero degrees (0°), and theta (θ) takes values from 0° to 180°. For case 2, φ and α take the values of 90° and 0° while θ is varied as before.

As with the results for the fixed orientation of the RFID reader in Section III, current distribution and RCS results are analyzed for the four investigated tags with the different outlined orientations of the incident plane wave in oblique polarization.

A. Surface current distribution analysis

The RFID reader orientation, like polarization, plays an important role. The current distribution results of the four realized tags for two selectively different orientations of the RFID reader (orientations of the incident plane wave) are depicted in Fig. 6.

Figures 6 (a) and (b) show the surface current distribution of Tag 1 for illuminating plane wave orientations $\varphi = 0°/\theta = 150°$ and $\varphi = 90°/\theta = 180°$, respectively. Figure 6 (a) shows the result at the resonance frequency of 12.96 GHz with a maximum current value of 0.031 A/m. The change of the incident plane wave elevation

Table 3: Comparison of different characteristics of the realized four iterations of Hilbert curve filling

Tag #	Iteration	Frequency Range (GHz)	Coding Capacity (bits)	Coding Spatial Capacity (bits/cm^2)	Coding Spectral Capacity (bits/GHz)	Coding Density (bits/GHz*cm^2)
1	1T	3.85-12.4	10	0.977	1.170	0.114
2	2T	3.21-17.08	16	1.563	1.154	0.113
3	3T	2.83-19.42	25	2.441	1.507	0.147
4	4T	4.21-18.78	26	2.539	1.784	0.174

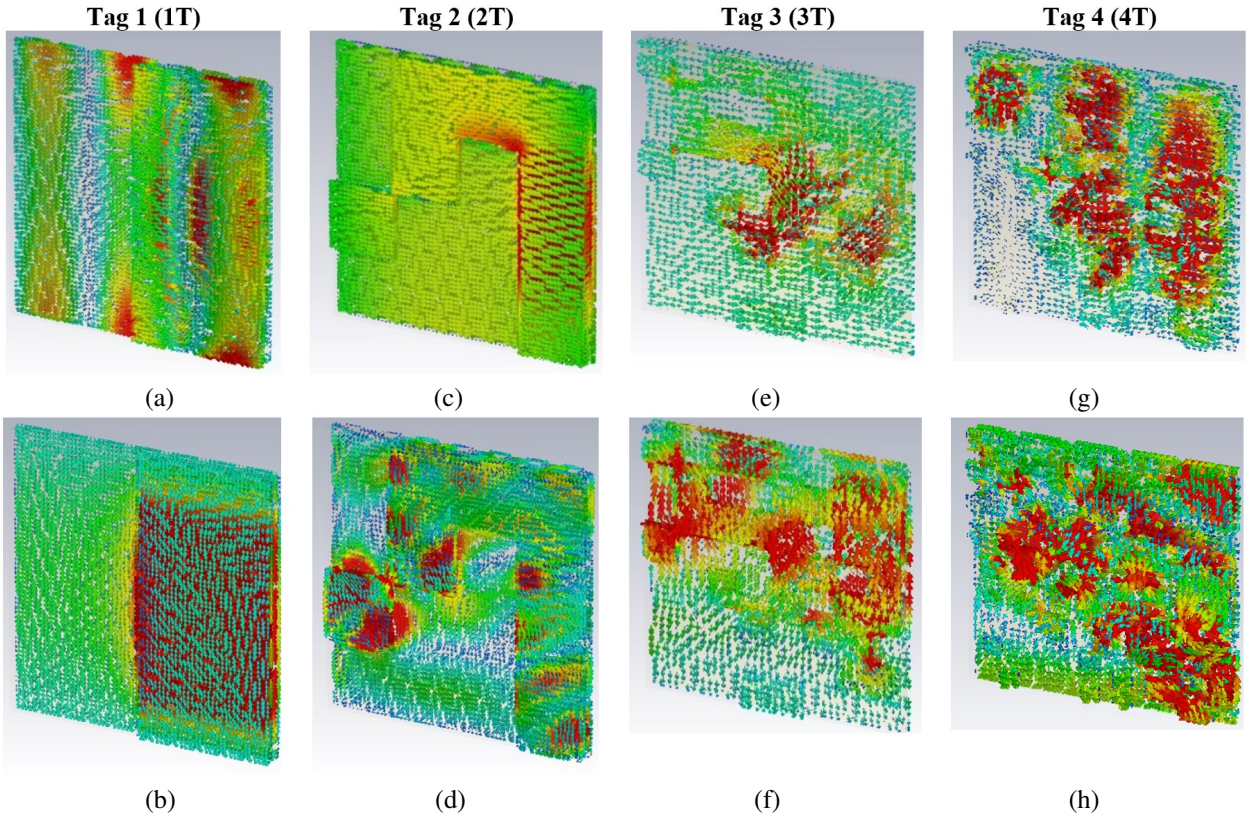

Fig. 6. The surface current distribution of four iterations of tags of Fig. 2 with the plane wave illumination angle of $\alpha = 0\circ$. (a) 1T at 12.96 GHz: $\varphi = 0\circ$ and $\theta = 150\circ$, J_{max} =0.031 A/m; (b) 1T at 2.13 GHz: $\varphi = 90\circ$ and $\theta = 180\circ$, J_{max} = 0.012 A/m; (c) 2T at 2.13 GHz: $\varphi = 0\circ$ and $\theta = 90\circ$, J_{max} = 0.032 A/m; (d) 2T at 13.41 GHz: $\varphi = 90\circ$ and $\theta = 180\circ$, J_{max} = 0.031 A/m; (e) 3T at 2.07 GHz: $\varphi = 0\circ$ and $\theta = 180\circ$, J_{max} = 0.026 A/m; (f) 3T at 3.75 GHz: $\varphi = 90\circ$ and $\theta = 140\circ$, J_{max} = 0.022 A/m; (g) 4T at 6.10 GHz: $\varphi = 0\circ$ and $\theta = 180\circ$, J_{max} =0.078 A/m; (h) 4T at 10.33 GHz: $\varphi = 90\circ$ and $\theta = 180\circ$, J_{max} =0.050 A/m.

angle to 90° and azimuth angle to 180° changes the resonance frequency of the tag to 2.13 GHz.

Figures 6 (c) and (d) represent the distributed current results of the 2T tag (Tag 2). Tag 2 exhibits the resonance frequency of 2.13 GHz for the plane wave having φ=0° and θ=90°, as depicted in Fig. 6 (c). It changes to 13.41 GHz when the reader is oriented to the positions of φ=90° and θ=180°, as shown in the changed pattern of the distributed current of Tag 2 in Fig. 6 (d). The comparison of the surface current distribution of the four tags in Figs. 6 (a-h) reveal significant variation with different orientations of the incident plane wave. Also, we can notice that the metallic shape of the tag impacts the induced current on the structure and thus produces a unique backscattered response for each tag, even for a fixed reader orientation.

B. RCS analysis

Figure 7 shows the RCS results of Tag 1 in oblique polarization for the two defined cases of elevation angles. The RCS results of the 1T tag for an incident plane wave with $\varphi = 0°$ and a change in azimuth angle from 0-180° with a step size of 10° are shown in Figs. 7 (a-c), respectively. The plane wave orientation of $\varphi = 0°$,

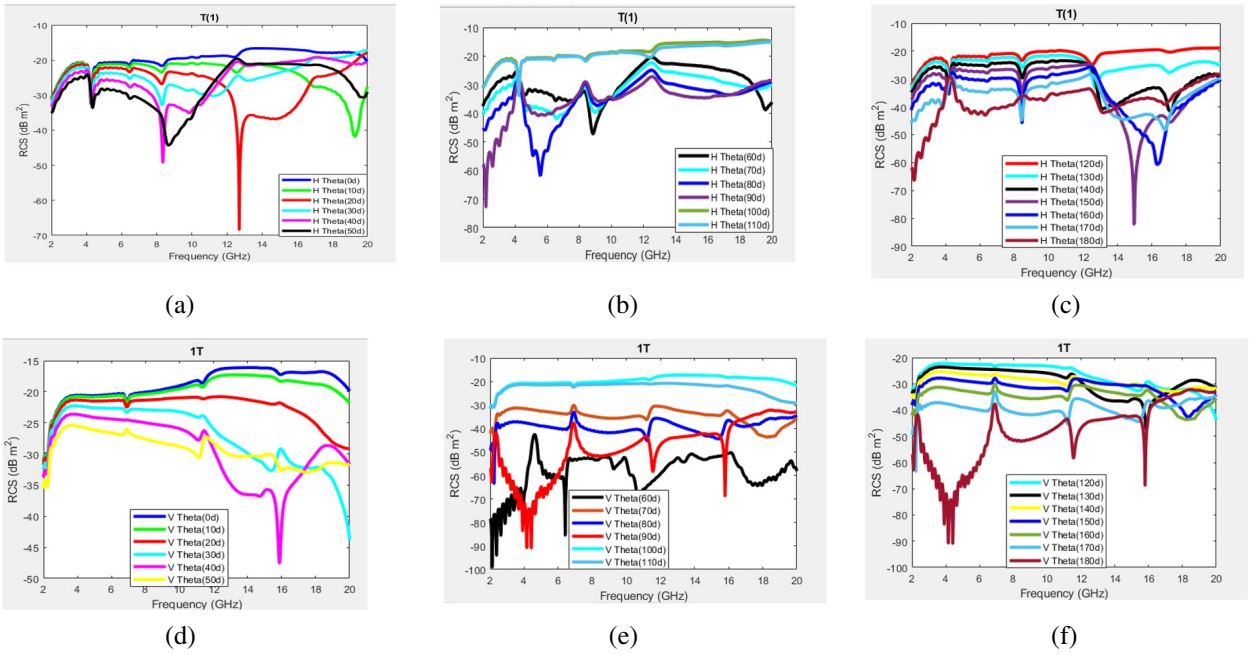

Fig. 7. RCS results of Tag 1 (1T) for oblique polarization with $\alpha = 0°$: (a) $\varphi = 0°$, θ = 0-50°; (b) $\varphi = 0°$, θ = 60-110°; (c) $\varphi = 0°$, θ = 110-180°; (d) $\varphi = 90°$, θ = 0-50°; (e) $\varphi = 90°$, θ = 60-110°; (f) $\varphi = 90°$, θ = 110-180°.

Table 4: Resonance frequency characteristics of Tag 1 (1T) for different angle of incidence of plane wave excitation in azimuth range for φ=90°

Theta	Resonance Frequencies (GHz)	# of Resonance Frequencies	Theta	Resonance Frequencies (GHz)	# of Resonance Frequencies
0°	4.25, 6.45, 8.30	3	100°	4.25, 6.43, 8.39	3
10°	4.27, 6.45, 8.26, 12.57, 19.26	5	110°	4.23, 6.41, 8.41, 12.42	4
20°	4.29, 6.45, 8.28, 12.69	4	120°	4.21, 6.41, 8.44, 12.51	4
30°	4.30, 6.46, 8.30	3	130°	4.21, 6.43, 8.44, 12.71, 17.03	5
40°	4.322, 6.5, 8.354	3	140°	4.20, 8.44, 13.11, 17.08	4
50°	4.34, 6.48, 8.66	3	150°	4.16, 8.44, 12.96, 17.12	4
60°	4.41, 8.86, 19.59	3	160°	4.12, 8.44, 16.31	4
70°	4.68, 6.59, 9.00	3	170°	3.40, 3.82, 8.43, 16.78	6
80°	5.11, 5.58, 9.18	3	180°	2.18, 2.58, 2.99, 6.30, 13.16, 16.76	4
90°	2.20, 2.61, 3.03	3			4

$\theta = 0°$ produces three significant resonance dips at 4.25 GHz, 6.45 GHz, and 8.30 GHz, respectively. The resonance frequencies change to 4.27 GHz, 6.45 GHz, 8.26 GHz, 12.57 GHz, and 19.26 GHz when θ is changed to 10°, as shown in Fig. 6 (a). Table 4 lists all significant resonances of Figs. 7 (a-c) waveforms for the complete sweep of azimuth angles with elevation angle (φ)=0°.

The heights of the resonances are recorded for the azimuth angles of 10° (5), 130° (5), and 180° (6). The metallic islands of the realized fractal tags are sensitive to the angle of incidence of the illuminating plane wave and thus show different resonance behavior even for a slight change in the orientation in the sweep range of the azimuth plane. The angular coding capacity for this case is computed using (5):

All resonance frequencies in oblique polarizations are added together for all different orientations of the reader (i.e. change in α, φ, θ). The coding spatial capacity, spectral capacity, and coding densities are calculated using (2)-(4). For this study, the focus is to demonstrate the proof-of-concept of the angular nature of the RFID reader on its detection performance. For the sake of simplicity, we assumed that angular encoding status was independent in this study. The coding capacity represent-

Table 5: Resonance frequency characteristics of Tag 1 (1T) for different angles of incidence of plane wave excitation in azimuth range for $\varphi = 90^\circ$

Theta	Resonance Frequencies (GHz)	# of Resonance Frequencies	Theta	Resonance Frequencies (GHz)	# of Resonance Frequencies
0°	6.90, 11.34, 15.91, 2.22	4	100°	6.90	2
10°	6.91, 11.36, 2.22	3	110°	6.91	1
20°	6.90, 2.22	2	120°	2.22, 6.90, 15.45	3
30°	2.22, 6.91, 15.41	3	130°	2.22, 11.13, 15.88	3
40°	2.22, 11.11, 15.88	3	140°	2.23, 11.16	2
50°	2.23, 11.14, 15.97	3	150°	2.23, 11.18, 18.36	3
60°	2.13, 2.38, 2.63, 2.88, 3.13, 3.40, 3.66, 3.93, 6.41, 9.25, 10.66, 13.39	12	160°	2.23, 11.20	2
70°	2.23, 11.20	2	170°	2.23, 2.58, 11.20, 15.43	4
80°	2.23, 2.58, 11.20, 15.43	4	180°	2.09, 2.56, 2.77, 3.01, 3.22, 3.46, 3.67, 3.91, 4.16, 4.41, 4.65, 4.86, 5.11, 11.56, 15.79	15
90°	2.09, 2.56, 2.77, 3.01, 3.22, 3.46, 3.67, 3.91, 4.16, 4.41, 4.65, 4.86, 11.56, 15.79	14			

ing the total number of resonance dips for this case is 70 bits, which produces the coding spatial capacity of 6.836 bits/cm^2.

$$\text{Coding Capacity}_{\text{ angular}} = \sum_{\theta=0^\circ}^{360^\circ} \sum_{\varphi=0^\circ}^{360^\circ} \sum_{\alpha=0^\circ}^{360^\circ} \text{All Resonance Frequencies (Oblique (Ob))}. \quad (5)$$

The RCS waveforms of the same tag in oblique polarization for the second case of zapping plane wave elevation angle, i.e., φ=90° are depicted in Figs. 7 (d-f). For the $\theta = 0^\circ$ orientation of the plane wave, the observed resonance frequencies are 6.90 GHz, 11.34 GHz, 15.91 GHz, and 2.22 GHz which are different when compared to the same case resonance of $\varphi = 0^\circ$. Similar observations can be made for the other cases of the azimuth angle by comparing the respective waveforms for each case in Fig. 7. The summary of the resonance frequencies for this case is given in Table 5. A larger number of resonances are obtained when the tag is excited with an incident plane wave with azimuth angles of 60° (12), 90° (14), and 180° (15). The total number of resonances for the complete azimuth sweep with $\varphi = 90^\circ$ is 85. The computed coding spatial capacity for this case is 8.301 bits/cm^2, which is higher than the first case, i.e., $\varphi = 0^\circ$.

Figure 8 illustrates the RCS waveforms of Tag 2 for the two analyzed cases of elevation angles. The first case results with $\varphi = 0^\circ$, and the change in θ is depicted in Figs. 8 (a-c). The observed resonance frequencies of the $\theta = 0^\circ$ waveform in Fig. 8 (a) are 3.21 GHz, 5.26 GHz, 6.32 GHz, 8.16 GHz, and 11 GHz. These frequencies change to 3.24 GHz, 5.29 GHz, 6.34 GHz, 8.36 GHz, and 11 GHz when the incident plane wave is oriented to $\varphi = 0^\circ$ and $\theta = 10^\circ$. Table 6 lists all resonance frequencies for Figs. 8 (a-c) waveforms. We can observe from Table 6 that the number and location of the resonance dip change with the variation in the incident plane wave orientations from $\theta = 0^\circ$ to $\theta = 180^\circ$ with a fixed $\varphi = 0^\circ$. The illuminating plane wave orientations of $\theta = 90^\circ$ and $\theta = 180^\circ$ produce maximum resonances of the metallic tag structures. The coding capacity for this first analyzed case of Tag 2 is 103 bits, which makes the coding spatial capacity 10.059 bits/cm^2.

Table 7 summarizes all observed resonance frequencies for Tag 2's second analyzed configuration i.e., φ=90° and sweeping of azimuth angle from 0° to 180°. Figures 8 (d-f) show the waveforms of the Table 6 results. The observed number of resonance frequencies when Tag 2 is illuminated with an incident plane wave of φ=90° and θ=0° is four (5.24 GHz, 6.36 GHz, 7.24 GHz, and 7.83 GHz). A total of nine resonance frequencies are noted for the case of θ=90°, θ=170°, and θ=180° for this case. The observed number of resonance frequencies for these three cases of θ=90°, θ=170°, and θ=180° is the highest in the complete sweep of azimuth angles. The coding capacity and coding spatial capacity for this second case of Tag 2 are 106 bits and 10.352 bits/cm^2, which are higher than case 1 of the same tag. It is noted that as the Tag 2 geometry is more irregular as compared to the Tag 1 geometry, a higher number of resonances and thus higher coding capacity are observed for Tag 2.

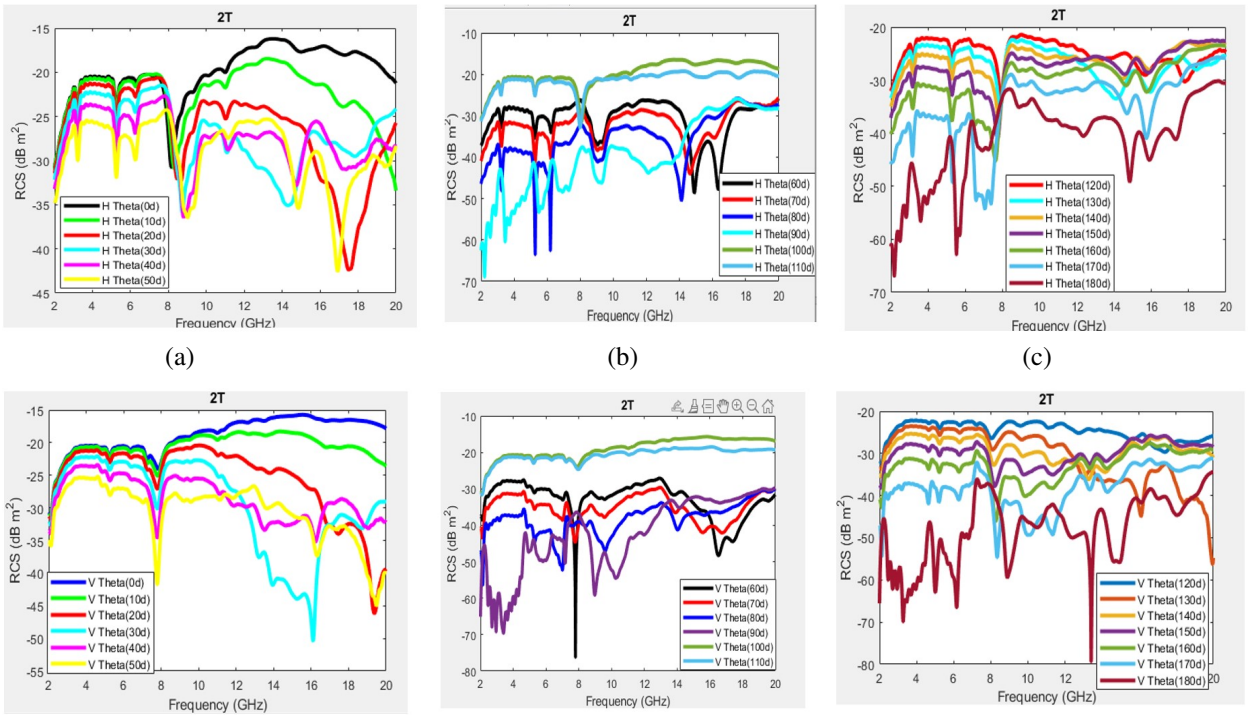

(a) (b) (c)

(d) (e) (f)

Fig. 8. RCS results of Tag 2 (2T) for oblique polarization with $\alpha = 0°$: (a) $\varphi = 0°$, θ = 0-50°; (b) $\varphi = 0°$, θ = 60-110°; (c) $\varphi = 0°$, θ = 110-180°; (d) $\varphi = 90°$, θ = 0-50°; (e) $\varphi = 90°$, θ = 60-110°; (f) $\varphi = 90°$, θ = 110-180°.

Table 6: Resonance frequency characteristics of Tag 2 for different angles of incidence of plane wave excitation in azimuth range for φ=0°

Theta	Resonance Frequencies (GHz)	# of Resonance Frequencies	Theta	Resonance Frequencies (GHz)	# of Resonance Frequencies
0°	3.21, 5.26, 6.32, 8.16, 11	5	100°	3.21, 5.26, 8.08	3
10°	3.24, 5.29, 6.34, 8.36, 11	5	110°	3.21, 5.26, 7.99	3
20°	3.22, 5.26, 6.28, 11.02, 17.52	5	120°	3.21, 5.26, 7.92, 15.68, 17.79	5
30°	3.22, 5.26, 6.27, 8.73, 11.09, 14.31	6	130°	3.21, 5.26, 7.87, 14.10, 15.93	5
40°	3.22, 5.26, 6.27, 8.80, 11.14, 14.74	6	140°	3.21, 5.28, 7.81, 14.49, 15.91	5
50°	3.22, 5.26, 6.27, 9.00, 11.16, 14.85, 16.92	7	150°	3.19, 5.29, 7.74, 14.60, 15.84	5
60°	3.22, 5.24, 6.25, 9.06, 14.89, 16.35	6	160°	3.17, 5.29,7.63, 14.65, 15.75	5
70°	3.22, 5.26, 6.23, 9.04, 14.64, 16.15	6	170°	3.17, 5.31, 6.57, 7.06, 7.38, 14.67, 15.73	7
80°	3.24, 5.28, 6.19, 9.07, 14.11	5	180°	2.18,2.50, 2.83, 3.60, 5.53, 12.35, 14.83, 15.90, 17.30	9
90°	2.22, 2.56, 2.88, 3.46,9.29	5			

Figures 9 and 10 show the RCS waveforms for both cases of elevation angle for Tags 3 and 4, respectively. The variations in the resonance characteristics of both tags could be noted by comparing the results of successive orientations. Tag 3 has six resonances at 6.97 GHz, 8.25 GHz, 9.13 GHz, 9.81 GHz, 10.39 GHz, and 15.28 GHz for $\varphi = 90°$ and $\theta = 0°$ incident plane wave orientation. While six dips at 6.55 GHz, 6.99 GHz, 8.17

Table 7: Resonance frequency characteristics of Tag 2 for different angles of incidence of plane wave excitation in azimuth range for φ=90°

Theta	Resonance Frequencies (GHz)	# of Resonance Frequencies	Theta	Resonance Frequencies (GHz)	# of Resonance Frequencies
0°	5.24, 6.36, 7.24, 7.83	4	100°	5.26, 7.22, 7.89	3
10°	5.26, 7.24, 7.81	3	110°	6.34, 7.22, 7.98	3
20°	5.26, 7.80, 17.46, 19.37	4	120°	5.24, 6.32, 8.03, 17.37	4
30°	5.26, 7.78, 13.20, 16.11, 18.74	5	130°	5.26, 6.34, 8.10, 12.98, 16.11,19.95	6
40°	5.28, 7.79, 13.52, 16.22	4	140°	4.65, 5.24, 6.32, 8.17,13.27, 14.20, 16.17	7
50°	5.28, 7.80, 13.59, 16.31, 19.48	5	150°	4.65, 5.24, 6.30, 8.21, 9.78, 11.32, 13.32	7
60°	5.29, 7.00, 7.80, 16.51, 17.41	5	160°	2.11, 4.65, 5.22, 6.28, 8.26, 9.85, 13.34, 14.29	8
70°	2.13, 5.29, 7.00, 7.78, 13.88, 15.57	6	170°	2.13, 4.65, 5.20, 6.28, 8.34, 10.14, 11.34, 13.34, 14.29	9
80°	2.13, 5.13, 7.00, 9.61, 14.04	5	180°	2.70, 2.95, 3.28, 5.01, 6.16, 8.89, 13.41,16.13, 18.07	9
90°	2.47, 2.70, 2.95, 3.40, 4.95, 7.17, 8.97, 10.26, 14.17	9			

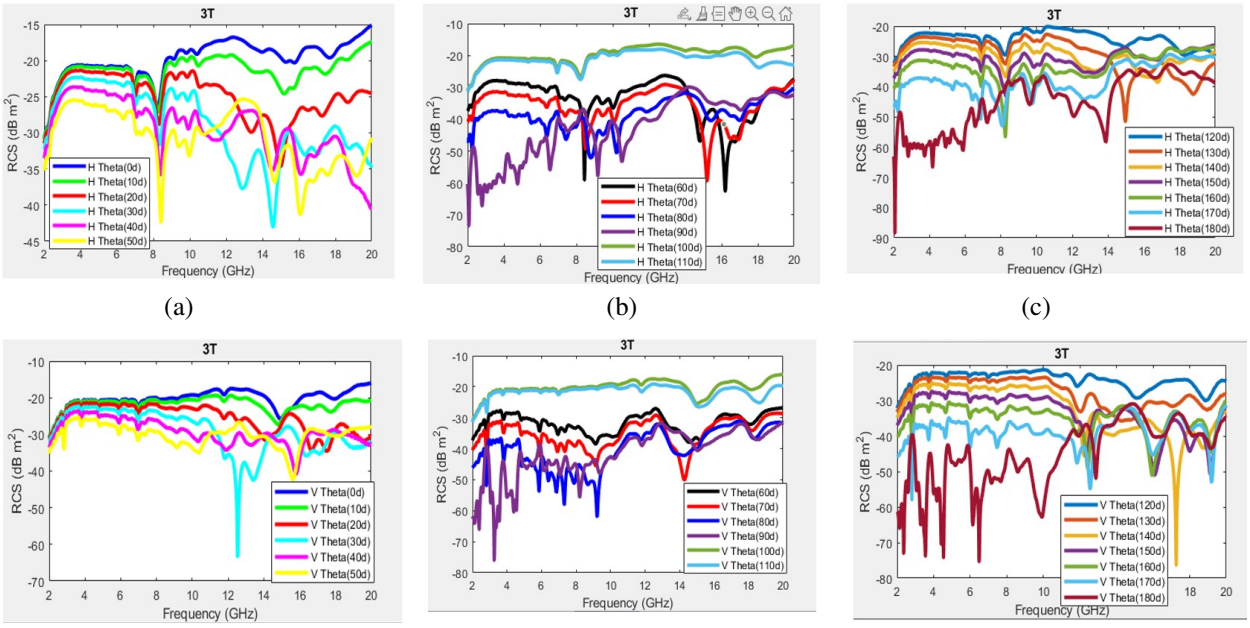

(a) (b) (c)

(d) (e) (f)

Fig. 9. RCS results of Tag 3 (3T) for oblique polarization with α=0°: (a) φ=0°, θ=0-50°; (b) φ=0°, θ=60-110°; (c) φ=0°, θ=110-180°; (d) φ=90°, θ=0-50°; (e) φ=90°, θ=60-110°; (f) φ=90°, θ=110-180°.

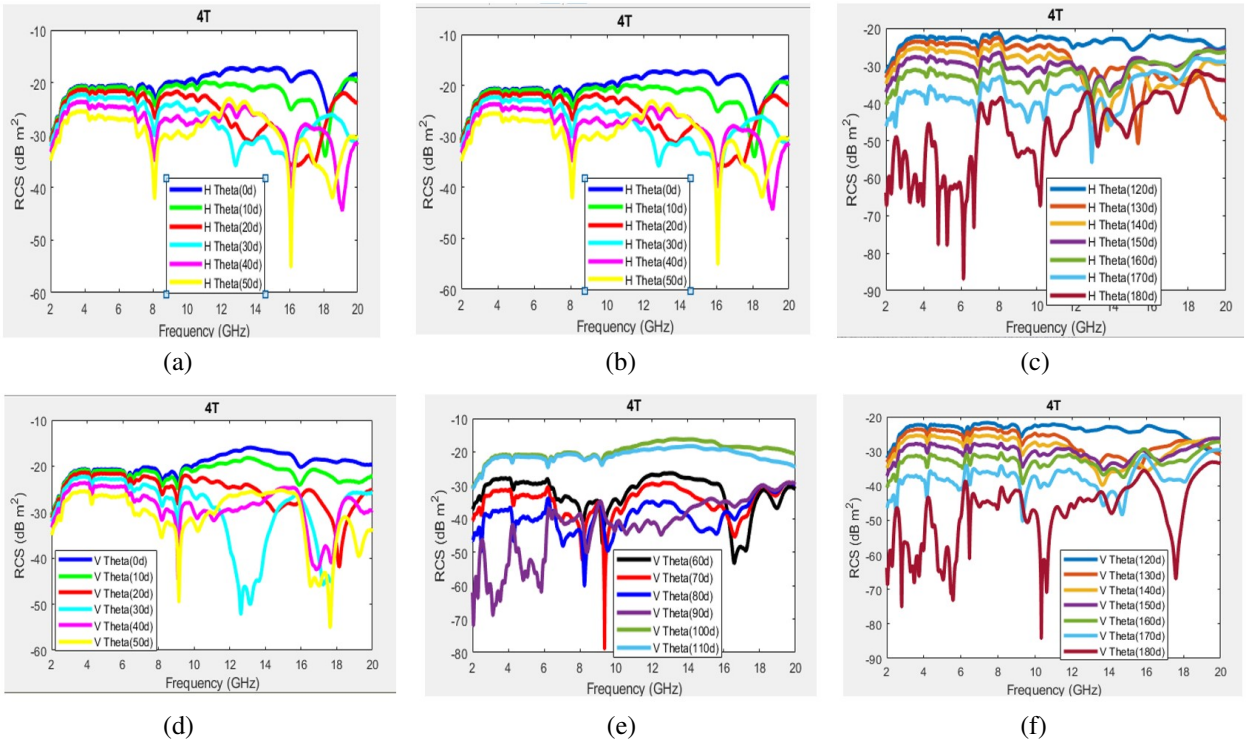

Fig. 10. RCS results of Tag 4 (4T) for oblique polarization with $\alpha = 0^\circ$: (a) $\varphi = 0^\circ, \theta = 0-50^\circ$; (b) $\varphi = 0^\circ, \theta = 60-110^\circ$; (c) $\varphi = 0^\circ, \theta = 110-180^\circ$; (d) $\varphi = 90^\circ, \theta = 0-50^\circ$; (e) $\varphi = 90^\circ, \theta = 60-110^\circ$; (f) $\varphi = 90^\circ, \theta = 110-180^\circ$.

Table 8: Comparison between the four realized chipless tags for two different cases of oblique polarization

# Tag	Frequency Range (GHz)	Coding Capacity (bits)	Coding Spatial Capacity (bits/cm^2)	Coding Spectral Capacity (bits/GHz)	Coding Density (bits/GHz x cm^2)
1-case 1	2.18-19.59	70	6.836	4.021	0.393
1-case 2	2.09-18.36	85	8.301	5.224	0.510
2-case 1	2.18-17.79	103	10.059	6.598	0.644
2-case 2	2.11-19.95	106	10.352	5.942	0.580
3-case 1	2.07-18.78	113	11.035	6.762	0.660
3-case 2	2.13-19.21	167	16.309	9.778	0.945
4-case 1	2.04-19.10	138	13.477	8.089	0.790
4-case 2	2.04-19.24	169	16.504	9.826	0.960

GHz, 10.55 GHz, 16.09 GHz, and 18.34 GHz in the RCS waveform of Tag 4 are observed for the same case as shown in Fig. 10 (a). As for Tag 2, the maximum number of resonances in RCS waveforms is noted for the zapping plane wave orientation of θ=180° for both configurations of elevation angle for both Tags 3 and 4, respectively. The tabular summaries of Figs. 9 and 10 results as in Tables 4–8 are not reported here for brevity. Table 8 presents the comparison of the performance of all analyzed tags for both cases of elevation angles (φ=0° for case 1 and φ=90° for case 2) in terms of their frequency range of the resonance spectrum, coding capacity (bits), coding spatial capacity (bits/cm^2), coding spectral capacity (bits/GHz), and coding density (bits/GHz x cm^2).

The coding capacities for Tags 3 and 4 are 113 bits and 167 bits and 138 bits and 169 bits for case 1 and case 2, respectively. It is observed that, as expected, the higher the irregularity in tag geometry, the higher the coding density. The highest coding capacity of 169 bits is noted for case 2 of Tag 4. The spectrum range of 2.04-19.24 GHz of Tag 4 is also wider as compared to less-fractal tags.

The observed coding spatial capacity for the second case of Tag 1 is 8.301 bits/cm^2, which changes to 10.352 bits/cm^2 for Tag 2, 16.309 bits/cm^2 for Tag 3, and

16.504 bits/cm^2 for Tag 4, respectively. A similar trend is observed for the increase in the fractal nature of the tag with increasing coding spectral capacity. The heights of the coding densities are observed for Tag 4, which are 0.790 bits/GHz x cm^2 and 0.960 bits/GHz x cm^2 for cases 1 and 2, respectively. The lowest levels of coding densities (0.393 bits/GHz x cm^2 and 0.510 bits/GHz x cm^2) are noted for Tag 1, owing to its simplified structure in the 1st iteration of the Hilbert curve filling algorithm. Due to its highly irregular tag geometry, Tag 4 performance is the best in terms of all compared parameters for all tags.

Table 8 results depict that the coding performance of the fractal (and even simple) tags can be comprehensively increased by incorporating the effect of reader orientation in the detection process. Lowering the step size of the azimuth sweep or adding more cases of elevation angle in the incident plane wave orientation will further enhance the coding capacity and coding density of the tag with the increased number of overall resonances in the analyzed spectral range.

The comparison of RCS results for realized fractal chipless RFID tags reveals that coding and detection performance is affected by reader orientation. The detection using different orientations of an RFID reader (different angles of incidence of the illuminating plane wave) further increases the security of the communication between the reader and the tag.

Although the fractal geometry of chipless RFID tags provides inherent advantages for secure communication, such tag responses are difficult to decode using a standard RFID reader. The detection of the tag based on the collected backscattered tag response with different orientations of the reader further increases the security of the communication as the backscattered RCS response is highly sensitive to slight variations in the reader orientation. The coding capacity and security performance of the realized tags could be further enhanced by incorporating the effect of the polarization factor into the analyzed RCS response of the tag along with the plane wave orientation factor without any change in the tag geometry.

V. CONCLUSION

The study has presented a comprehensive analysis of the impact of the RFID reader orientation (angle of incidence of an illuminating plane wave) on the sensing and detection capabilities of the realized fractal chipless RFID tags. The analysis is performed on four irregular chipless RFID tags developed based on the Hilbert curve filling algorithm for the two different elevation angles of an incident plane wave in oblique polarization. The analysis suggested that higher coding and detection performance of the tag in terms of coding capacity, coding spatial capacity, coding spectral capacity, and coding density is obtained when the aggregated backscattered RCS responses of the tag are analyzed in the azimuth range of 0° to 180° for two cases of elevation angles (0° and 90°). The detection based on the proposed aggregated analysis approach not only enhanced the coding and sensing performance of the tag but also made the communication highly secure. The proposed strategy could be used for the development of future highly secured RFID-based communication systems for smart cities, confidential documents, and Internet of Things (IoT) applications.

ACKNOWLEDGMENT

This project was funded by the Deanship of Scientific Research (DSR), King Abdulaziz University, under grant No. (21-135-35-HiCi). The authors, therefore, acknowledge the technical and financial support of KAU.

REFERENCES

[1] Q. H. Sultan and A. M. Sabaawi, "Design and implementation of improved fractal loop antennas for passive UHF RFID tags based on expanding the enclosed area," *Progress in Electromagnetics Research C*, vol. 111, pp. 135-145, 2021.

[2] M. Borgese, S. Genovesi, G. Manara, and F. Costa, "Radar cross section of chipless RFID tags and BER performance," *IEEE Transactions on Antennas and Propagation*, vol. 69, no. 5, pp. 2877-2886, 2021.

[3] H. Rmili, B. Oussama, J. Yousaf, B. Hakim, R. Mittra, T. Aguili, and S. Tedjini, "Robust detection for chipless RFID tags based on compact printable alphabets," *Sensors*, vol. 19, no. 21, p. 4785, 2019.

[4] C. Herrojo, M. Moras, F. Paredes, A. Nunez, E. Ramon, J. Mata-Contreras, and F. Martin, "Very low-cost 80-bit chipless-RFID tags inkjet printed on ordinary paper," *Technologies*, vol. 6, no. 2, 2018.

[5] K. Issa, Y. Alshoudokhi, M. Ashraf, M. Alshareef, H. Behairy, S. Alshebeili, and H. Fathallah, "A high-density L-shaped backscattering chipless tag for RFID bistatic systems," *International Journal of Antennas and Propagation* vol. 2018, p. 10, 2018.

[6] L. M. Arjomandi, G. Khadka, Z. Xiong, and N. C. Karmakar, "Document verification: A cloud-based computing pattern recognition approach to chipless RFID," *IEEE Access*, vol. 6, pp. 78007-78015, 2018.

[7] H. Rmili, D. Oueslati, L. Ladhar, and M. Sheikh, "Design of a chipless RFID tags based on natural fractal geometries for security applications," *Microwave and Optical Technology Letters*, vol. 58, no. 1, pp. 75-82, 2016.

[8] H. Huang and L. Su, "A compact dual-polarized chipless RFID tag by using nested concentric square loops," *IEEE Antennas and Wireless Propagation Letters*, vol. 16, pp. 1036-1039, 2017.

[9] M. Polivka, J. Havlicek, M. Svanda, and J. Machac, "Improvement in robustness and recognizability of RCS response of U-shaped strip-based chipless RFID tags," *IEEE Antennas and Wireless Propagation Letters*, vol. 15, pp. 2000-2003, 2016.

[10] O. Necibi, S. Beldi, and A. Gharsallah, "Design of a chipless RFID tag using cascaded and parallel spiral resonators at 30 GHz," in *2015 2nd World Symposium on Web Applications and Networking (WSWAN)*, pp. 1-5, 2015.

[11] J. Y. Mohammad, N. Zaqumi, M. Zarouan, M. A. Hussaini, and H. Rmili, "Passive fractal chipless RFID tags based on cellular automata for security applications," *Applied Computational Electromagnetics Society (ACES) Journal*, vol. 36, no. 5, pp. 559-567, May 2021.

[12] E. Motovilova and S. Y. Huang, "Hilbert curve-based metasurface to enhance sensitivity of radio frequency coils for 7-T MRI," *IEEE Transactions on Microwave Theory and Techniques*, vol. 67, no. 2, pp. 615-625, 2019.

[13] M. E. Mousa, H. H. Abdullah, and M. E. d. A. El-Soud, "Compact chipless RFID tag based on fractal antennas and multiple microstrip open stub resonators," in *2018 Progress in Electromagnetics Research Symposium (PIERS-Toyama)*, pp. 1332-1338, 2018.

[14] L. Wang, T. Liu, J. Sidén, and G. Wang, "Design of chipless RFID tag by using miniaturized open-loop resonators," *IEEE Transactions on Antennas and Propagation*, vol. 66, no. 2, pp. 618-626, 2018.

[15] M. Alibakhshi-Kenari, M. Naser-Moghadasi, R. A. Sadeghzadeh, B. S. Virdee, and E. Limiti, "Dual-band RFID tag antenna based on the Hilbert-curve fractal for HF and UHF applications," *IET Circuits, Devices & Systems*, vol. 10, no. 2, pp. 140-146, 2016.

[16] N. A. Murad, M. Esa, M. F. M. Yusoff, and S. H. A. Ali, "Hilbert curve fractal antenna for RFID application," in *2006 International RF and Microwave Conference*, pp. 182-186, 2006.

[17] J. McVay, A. Hoorfar, and N. Engheta, "Space-filling curve RFID tags," in *2006 IEEE Radio and Wireless Symposium*, pp. 199-202, 2006.

[18] L. Velho and J. D. M. Gomes, "Digital halftoning with space filling curves," *Proc. Of the 18th ann. Conf. on Computer Graphics and Interactive Techniques*, vol. 25, no. 4, pp. 81-90, 1991.

[19] Y. Watanabe and H. Igarashi, "Shape optimization of chipless RFID tags comprising fractal structures," *International Journal of Applied Electromagnetics and Mechanics,* vol. 52, no. 1-2, pp. 609-616, 2016.

Muntasir Sheikh received his B.Sc. from King Abdulaziz University, Saudi Arabia, in Electronics and Communications Engineering, M.Sc. in RF Communications Engineering from the University of Bradford, UK, and Ph.D. in Electromagnetics Engineering and Applications from the University of Arizona, USA. Since then, he has been teaching in the Electrical and Computer Engineering Dept. in KAU. His research interests are antenna theory and design, radar applications, and electromagnetic metamaterials.